

**FACULTY
OF MATHEMATICS
AND PHYSICS**
Charles University

BACHELOR THESIS

David Kománek

Heat conduction in interstellar bubbles

Astronomical Institute of Charles University

Supervisor of the bachelor thesis: Mgr. Richard Wunsch, Ph.D.

Study programme: Physics

Study branch: Physics

Prague 2023

I declare that I carried out this bachelor thesis independently, and only with the cited sources, literature and other professional sources. It has not been used to obtain another or the same degree.

I understand that my work relates to the rights and obligations under the Act No. 121/2000 Sb., the Copyright Act, as amended, in particular the fact that the Charles University has the right to conclude a license agreement on the use of this work as a school work pursuant to Section 60 subsection 1 of the Copyright Act.

In date

Author's signature

Words cannot express my gratitude to my supervisor Mgr. Richard Wünsch, Ph.D. His insights and suggestions have been instrumental in this work. I am grateful to have the opportunity to work under his guidance. I would also like to thank my family, especially my parents and brothers, for their unending love, support, and encouragement. Without them, I could not have undertaken this journey.

The software used in this work was developed in part by the DOE NNSA- and DOE Office of Science-supported Flash Center for Computational Science at the University of Chicago and the University of Rochester.

This work was supported by the Ministry of Education, Youth and Sports of the Czech Republic through the e-INFRA CZ (ID:90140)

Title: Heat conduction in interstellar bubbles

Author: David Kománek

Department: Astronomical Institute of Charles University

Supervisor: Mgr. Richard Wünsch, Ph.D., Astronomical Institute, Academy of Sciences of the Czech Republic

Abstract: We present the HECTOR sub grid model, a semi-analytical code capable of calculating 1D stationary solutions around contact discontinuities including radiative cooling and heat conduction. We use HECTOR to correct unresolved contact discontinuities in FLASH simulations of interstellar bubbles driven by stellar winds. Low resolution simulations underestimate the mass of hot ($T > 3.5 \times 10^5$ K) gas in the bubbles by a factor of $\sim 2 - 3$. With HECTOR we are able to reproduce the results of high resolution simulations at lower resolutions. Our results are in agreement with the semi-analytical solution by Weaver et al. [1977]. Unlike Weaver et al. [1977] solution, HECTOR is much more general and can be used in a wide variety of 1D or 3D simulations.

Keywords: bubbles, heat conduction, hydrodynamics, stellar winds, astrophysics

Contents

Introduction	2
1 Interstellar bubbles	3
1.1 Structure	3
1.2 Weaver solution	3
2 Numerical model	7
2.1 FLASH hydrodynamic code	7
2.2 Radiative cooling	8
2.3 Heat conduction	9
2.4 Cooling-conduction interaction	10
3 HECTOR – HEat Conduction correcTOR	12
3.1 Semi-analytical model	12
3.2 Correcting FLASH solution	14
4 Results	17
4.1 Setup	17
4.2 Single star	17
4.3 Star cluster	18
Summary	22
Bibliography	23

Introduction

The goal of this work is to improve handling of heat conduction and cooling in FLASH simulations, especially at contact discontinuities. This is particularly important for calculating properties of interstellar bubbles, because heat conduction and cooling are the main drivers of the evaporation of the shell gas into the bubble interior thus changing density and temperature of the accumulated gas. This for instance affects how quickly the interstellar bubbles grow and that, in turn, how efficient is the stellar feedback in regulating the collapse of molecular clouds.

The correct handling of interstellar bubbles is vital for complex simulations of the interstellar medium in galaxies, specifically in project SILCC (Simulating the Life-Cycle of molecular Clouds)—a large international collaboration aiming to improve our understanding of the star-gas cycle in galaxies (Walch et al. [2015]) which studies molecular clouds in regions of disc galaxies including the effects of self-gravity, magnetic fields, heating and cooling at different gas metallicities, molecule formation and dissociation, and stellar feedback. Figure 1.4 shows a SILCC run including supernovae, stellar winds, ionising radiation and cosmic rays.

In section 1 we go over the structure and evolution of interstellar bubbles. In section 2 we describe the numerical code used to simulate interstellar bubbles. In section 3 we introduce the HECTOR sub grid model we have developed to improve unresolved contact discontinuities in FLASH simulations. In section 4 we present two tests: we use the HECTOR code to simulate interstellar bubbles driven by stellar winds. We compare our results to the solution obtained by Weaver et al. [1977]; additionally, we discuss differences between 1D and 3D simulations at various resolutions. Finally, we summarize our work in Summary.

1. Interstellar bubbles

Massive stars with stellar winds reaching terminal velocities of thousands of kilometers per second can create cavities filled with hot gas in the surrounding interstellar medium. These structures are known as interstellar bubbles. An example is the Bubble Nebula shown in figure 1.1. There have been many observational studies interested in interstellar bubbles, including Deharveng et al. [2010] and Churchwell et al. [2006]. The structure and dynamical evolution of interstellar bubbles have been studied in theoretical works, including Castor et al. [1975], Weaver et al. [1977], Toalá and Arthur [2011], and Geen et al. [2015].

1.1 Structure

The structure of an interstellar bubble is shown in figure 1.2. The innermost region (a) is called the free wind region because it consists of the freely expanding, high-velocity stellar wind with temperatures in the thousands of kelvins. The wind then reaches the reverse shock (R_1) where most of its kinetic energy is converted to thermal energy. The wind forms region (b) of the bubble with high pressure and temperatures reaching 10^7 K. Due to the high pressure, the shocked wind expands and forms a high-density shell of swept-up interstellar medium, denoted by (c) in the sketch. The interface between regions (b) and (c) is called the contact discontinuity (R_c) and is characterized by a sudden rise in density, a drop in temperature, and a constant pressure across. The bubble is surrounded by region (d) of the ambient interstellar gas. The outer discontinuity between regions (c) and (d) is called the shock front (R_2).

1.2 Weaver solution

In a plasma with a temperature gradient, heat is conducted from the hotter to the colder parts. This process is mostly dominated by electrons because its efficiency is inversely proportional to particle mass.

Avedisova [1972] and Weaver et al. [1977] developed a similarity solution for the structure and the evolution of regions (b) and (c) of interstellar bubbles driven by a stellar wind source with a constant mechanical luminosity. The solution for the shocked stellar wind region (b) can be written using functions of a single dimensionless parameter

$$\xi = \frac{r}{R_2(t)}, \quad (1.1)$$

where r is the distance from the star and t is the time since the wind expansion began. The dimensionless functions $U(\xi)$, $G(\xi)$, and $P(\xi)$ of the self-similar flow are defined as $v(r) \propto U(\xi)$, $\rho(r) \propto G(\xi)$, and $p(r) \propto P(\xi)$, where v is the wind velocity, ρ is the density, and p is the pressure. At early times, when radiative cooling of the hot gas is not significant, an adiabatic approximation can be used. At later times, radiative losses and heat conduction should be included, Weaver et al. [1977] give the similarity solution that includes the above processes. This solution is derived from the result by Cowie and McKee [1977] that the flux



Figure 1.1: Bubble Nebula (NGC 7635) captured in visible light by the Hubble Space Telescope. The colors correspond to blue for oxygen, green for hydrogen, and red for nitrogen. The bubble is about 2 pc across and forms around a Wolf-Rayet star 2200 pc from the Sun. Source: NASA Goddard Space Flight Center.

of the thermal energy due to the heat conduction and cooling is exactly balanced by the flux of the mechanical energy due to the shell evaporation. The evolution of an interstellar bubble calculated using the Weaver solution is shown in figure 1.3 where R_1 is the radius of the reverse shock, R_2 is the radius of the shock front, V_2 is the velocity of the shock front, E_b , M_b , and L_b are the energy, mass, and luminosity of the shocked stellar wind in region (b). We can see that at later times, V_2 starts to decrease more rapidly as the pressure from the surrounding interstellar medium dominates over the pressure inside the bubble.

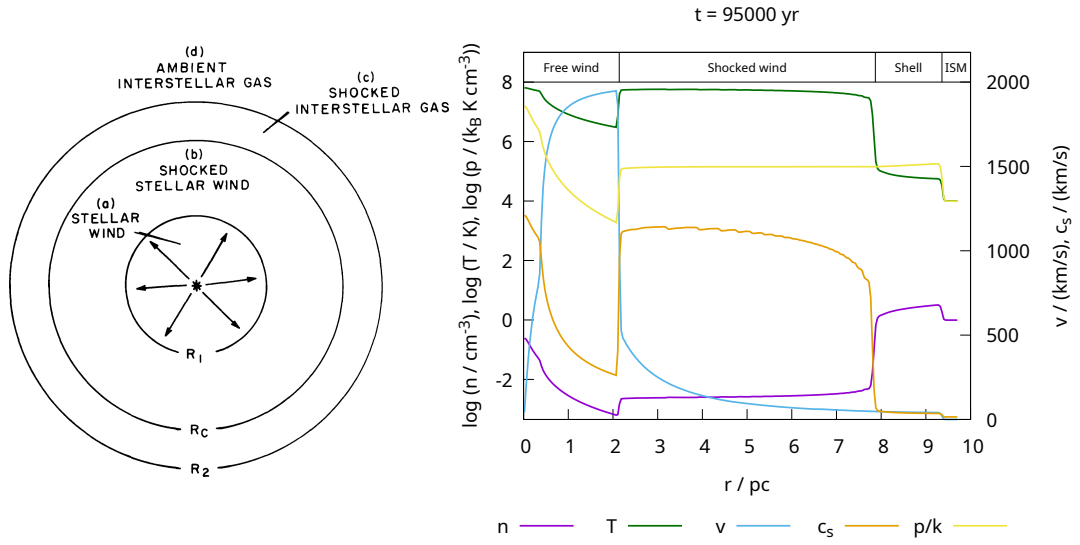


Figure 1.2: The left panel shows a sketch of the structure of the stellar bubble, source: Weaver et al. [1977]. The right panel shows the radial profiles of the hydrodynamic quantities in the interstellar bubble with the mechanical luminosity of the stellar wind, $L_w = 1.27 \times 10^{36}$ erg, the terminal velocity, $v_\infty = 2000 \text{ km s}^{-1}$, and the density of the interstellar medium, $n_0 = 1 \text{ cm}^{-3}$ with no cooling and no heat conduction.

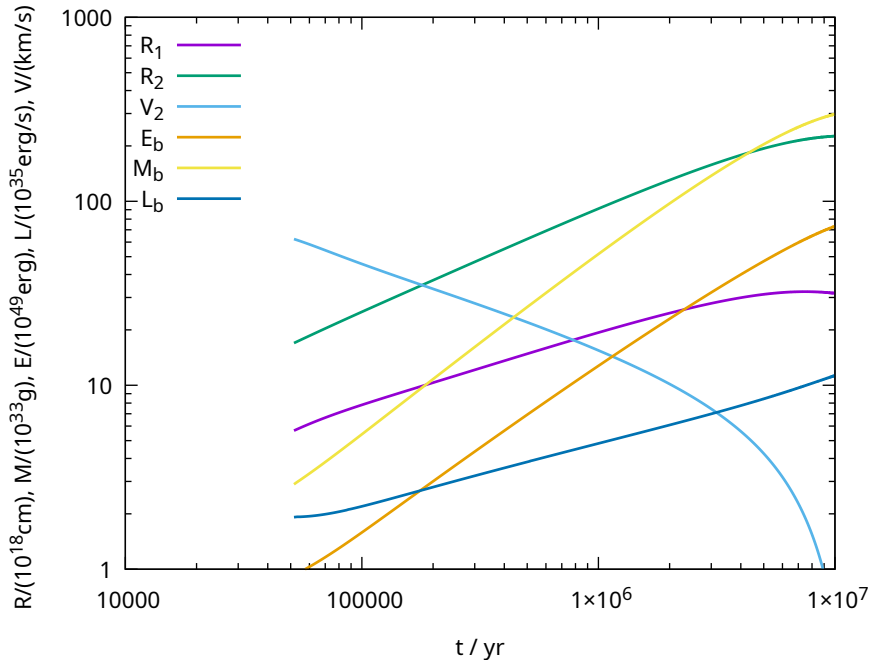


Figure 1.3: Evolution of a bubble with $L_w = 1.27 \times 10^{36}$ erg and $n_0 = 1 \text{ cm}^{-3}$ when the exterior is an H II region at $T = 8000 \text{ K}$. Individual lines show the radius of the reverse shock, R_1 (magenta), the radius of the outer shock front, R_2 (green), the shock velocity, V_2 (light blue), the thermal energy in region (b), E_b (orange), the mass of the hot gas in region (b), M_b (yellow), and the luminosity of region (b), L_b (dark blue).

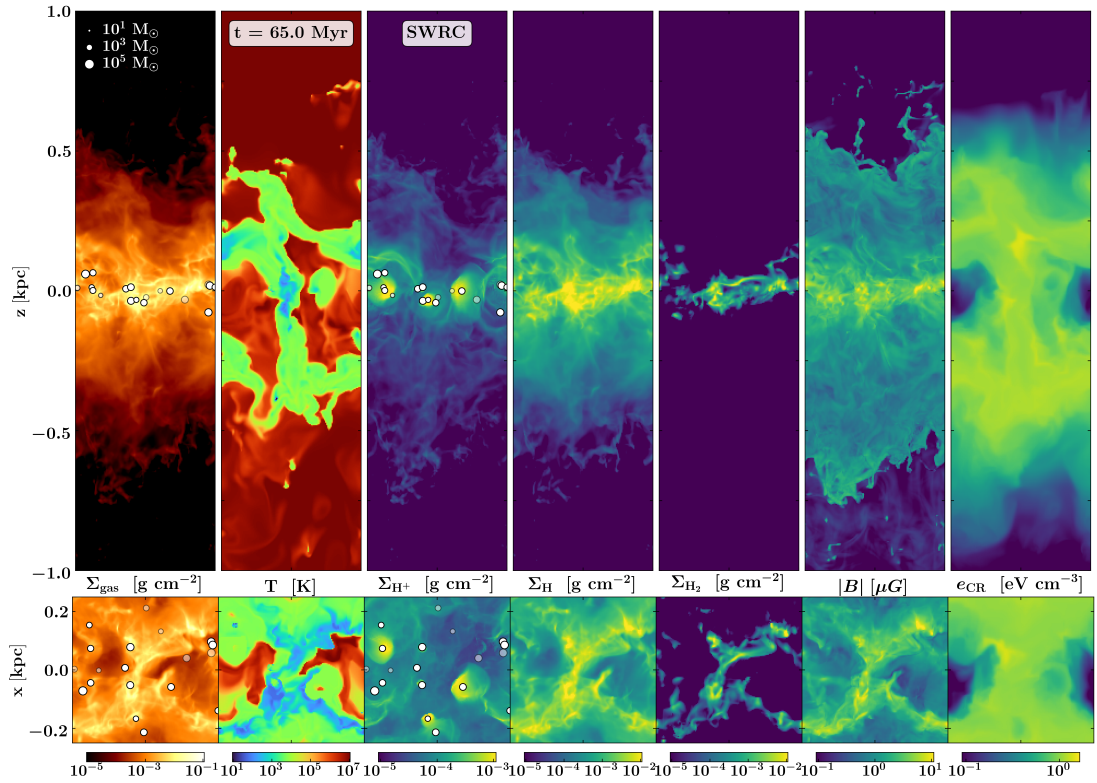


Figure 1.4: A SILCC run, including supernovae, stellar winds, UV radiation, and cosmic rays at $t = 65$ Myr. The computational domain size is $0.5 \text{ kpc} \times 0.5 \text{ kpc} \times 4 \text{ kpc}$. Periodic boundary conditions are used in the x and y directions, and outflow boundary conditions are used in the z direction. Edge-on (top row) and face-on (bottom row) views show by color the following quantities (from left to right): the total gas column density, slices through the center of the simulation with the temperature, the ionized hydrogen column density, the atomic hydrogen column density, the molecular hydrogen column density, the density-weighted column of the magnetic field strength, and slices through the center of the simulation with the cosmic ray energy density. The circles in the first and third panels indicate star clusters. Source: Rathjen et al. [2021]

2. Numerical model

Here we describe the numerical code used for the hydrodynamic simulations of interstellar bubbles presented in this thesis. We will review the core equations as well as the modules used to implement radiative cooling and heat conduction. We will then perform simulations of simple problems to assess the validity of the results obtained with the code.

2.1 Flash hydrodynamic code

FLASH 4.6.2 (Fryxell et al. [2000]) is a three-dimensional hydrodynamic code written in Fortran 90 and C. It is parallelized using the Message Passing Interface library (Message Passing Interface Forum [2021]) and supports adaptive mesh refinement using the Paramesh library (Olson et al. [1999]).

The hydrodynamic module solves the following equations for compressible gas using the piecewise parabolic method (Colella and Woodward [1984]),

$$\frac{\partial \rho}{\partial t} + \nabla \cdot \rho \mathbf{v} = q_m, \quad (2.1)$$

$$\frac{\partial \rho \mathbf{v}}{\partial t} + \nabla \cdot \rho \mathbf{v} \mathbf{v} = \rho \mathbf{g} - \nabla P - q_m \mathbf{v}, \quad (2.2)$$

$$\frac{\partial \rho E}{\partial t} + \nabla \cdot (\rho E + P) \mathbf{v} = \rho \mathbf{v} \cdot \mathbf{g} - Q + q_e - \nabla q_c, \quad (2.3)$$

where ρ , \mathbf{v} , and P are the fluid density, velocity, and pressure, respectively, \mathbf{g} is the acceleration due to gravity, Q is the cooling term discussed in section 2.2, q_m is the mass deposition rate, q_e is the energy deposition rate, q_c is the heat conduction flux, and E is the sum of internal and kinetic energy per unit mass

$$E = \frac{P}{(\gamma - 1)\rho} + \frac{v^2}{2} \quad (2.4)$$

where γ is the ratio of specific heats. For the sake of simplicity, we neglected the gravitational acceleration \mathbf{g} . This is safe in the early phases of the bubble evolution when other accelerations (e.g., due to the pressure force) dominate. In addition to equations 2.1–2.3 we need the equation of state of the ideal gas

$$P = \frac{k_B \rho T}{\mu m_H}, \quad (2.5)$$

where μm_H is the mean mass per particle with $\mu = 0.609$ corresponding to the ionized gas with the chemical composition of the Sun, T is the temperature, and k_B is the Boltzmann constant.

The simulations in this thesis were performed on the Karolina supercomputer operated by IT4Innovations and on the Virgo cluster operated by the Astronomical Institute of the Czech Academy of Sciences. We used about 50000 core hours.

2.2 Radiative cooling

Hot gas in regions (b) and (c) cools by emitting electromagnetic radiation, and the resulting energy losses significantly modify the bubble evolution. Therefore, we take this effect into account. We assume that the number densities of electrons and ions n_i and n_e , respectively, are equal and given by

$$n_i = n_e = \frac{\rho}{\mu_i m_H}, \quad (2.6)$$

where $\mu_i m_H$ is the mean mass per ion with $\mu_i = 1.273$ and ρ is the density. The cooling rate is given by the equation

$$Q = n_i n_e \Lambda(T), \quad (2.7)$$

where $\Lambda(T)$ is a cooling function calculated by Schure et al. [2009] and shown in figure 2.1.

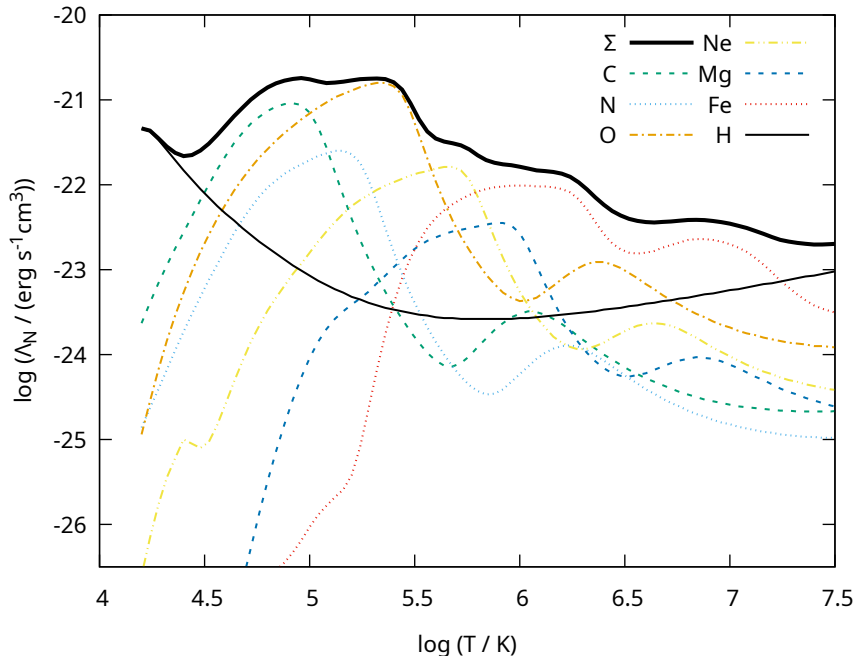


Figure 2.1: Contributions of different elements to the Schure et al. [2009] cooling function. The solid black line shows the total cooling function. The plot is shown for the solar chemical composition used throughout this work; however, it can be easily modified for any other composition by scaling the species composition.

In interstellar bubbles, radiative cooling affects regions (b) and (c). The latter one (shell of the accreted ISM) cools rapidly at a given time and collapses into a thin shell. The calculation of this process is relatively straightforward within the framework of the adopted assumptions, and we therefore focus here on the calculation of the energy losses from region (b). The highest radiative losses occur at the contact discontinuities, where the cooling function peaks. This reduces the thermal energy flux, which is canceled by the mechanical energy flux (Cowie and McKee [1977]). As a result, less gas flows into the bubble. This reduces the mass of the wind accumulated in a bubble.

2.3 Heat conduction

Heat conduction falls into the category of diffusion problems. FLASH includes several diffusion solvers that can be divided into two groups: explicit and implicit. Flux-based solvers are explicit diffusion solvers, and they work by calculating the heat fluxes at the cell faces. Unfortunately, these solvers are not fast enough for our applications because they have to limit the time step of the simulation to ensure the stability, and this would lead to time steps by several orders of magnitude smaller than those required by the hydrodynamic solver. On the other hand, the implicit solvers are much faster, because they do not constrain the time step, but they can be inaccurate if the heat fluxes are too large.

To evaluate whether the diffuse and conduction units in FLASH are working correctly, we calculated the evolution of the 1D delta distribution in temperature. The solution of equation

$$k\Delta T(x, t) = \frac{\partial T(x, t)}{\partial t}, \quad (2.8)$$

where $k = 1000 \text{ cm}^2/\text{s}$ is the heat conductivity and $x \in \mathbb{R}$, $t/\text{s} \in [0, \infty)$ are space and time coordinates, respectively, for the initial conditions

$$T(x, t = 0 \text{ s}) = N\delta(x), \quad (2.9)$$

is the Gaussian heat kernel multiplied by a normalization constant $N > 0 \text{ K cm}$

$$T(x, t) = \frac{N}{\sqrt{4\pi kt}} \exp\left(-\frac{x^2}{4kt}\right). \quad (2.10)$$

Figure 2.2 shows a FLASH simulation with initial conditions set to the solution 2.10 with $t = 5 \times 10^{-3} \text{ s}$ and hydrodynamics disabled. In the right panel we can see this simulation at a later time compared to the analytical solution 2.10. We conclude that FLASH solutions for simple problems are consistent with analytical solutions.

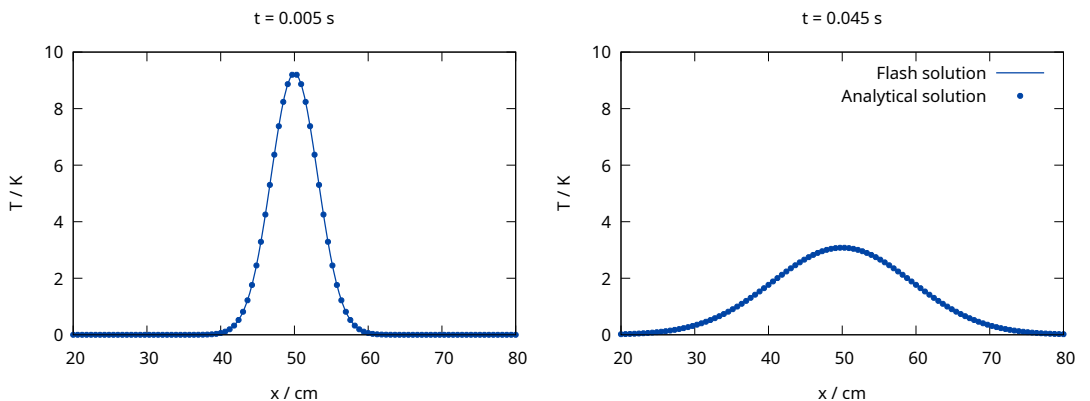


Figure 2.2: Heat conduction test in FLASH with hydrodynamics disabled compared to the analytical solution 2.10. Initial conditions were set to the fundamental solution of the heat equation 2.10 at $t = 5 \times 10^{-3} \text{ s}$.

The heat conduction coefficient for hydrogen plasma is given by (Spitzer [1962])

$$\kappa \approx 4.6 \times 10^{13} \left(\frac{T}{10^8 \text{ K}} \right)^{\frac{5}{2}} \left(\frac{\ln \Lambda}{40} \right)^{-1} \text{ erg s}^{-1} \text{ cm}^{-1} \text{ K}^{-1} = KT^{\frac{5}{2}}, \quad (2.11)$$

where the Coulomb logarithm quantifies the effect of small-angle collisions dominating over large-angle collisions and can be written as

$$\ln \Lambda = \int \frac{d\chi}{\chi}, \quad (2.12)$$

where χ is the angle of deflection. The Coulomb logarithm is a weak function of number density and electron temperature but can be treated as a constant (Cowie and McKee [1977]). We will use $\ln \Lambda \approx 40$, so the constant $K = 4.6 \times 10^{-7} \text{ erg s}^{-1} \text{ cm}^{-1} \text{ K}^{-7/2}$. Weaver et al. [1977] used an older formula giving $K = 1.2 \times 10^{-6} \text{ erg s}^{-1} \text{ cm}^{-1} \text{ K}^{-7/2}$, El-Badry et al. [2019] used $\ln \Lambda = 30$ giving $K \doteq 6.1 \times 10^{-7} \text{ erg s}^{-1} \text{ cm}^{-1} \text{ K}^{-7/2}$.

In the interstellar bubbles, the heat is conducted from the shocked stellar wind (region b) to the warm or cold shell (region c) where the energy is radiated away by the electromagnetic waves (cooling). In this way, the thermal energy and pressure in region (b) are reduced, resulting in a slower expansion of the bubble. In addition, the outward flux of the thermal energy is balanced by the inward flux of the mechanical energy, resulting in the evaporation of the shell into the hot shocked wind region. This increases the mass of region (b).

2.4 Cooling–conduction interaction

Figure 2.3 shows the mass of the accumulated shocked stellar wind in region (b). As we have discussed above, we can see that heat conduction increases while cooling decreases the evaporation of gas from the shell. The two runs that include the heat conduction show significantly more hot gas in the bubble interior than the two runs that do not. The run that includes both heat conduction and cooling has slightly less hot gas in the bubble interior than the run that includes only the heat conduction. We can also see that after an initial increase at the beginning of the simulation there is a brief period when the mass of the bubble decreases. This happens because the structure is not yet fully developed and the identification of region (b) does not work correctly. We are therefore interested in the later stages when mass is being accumulated.

Figure 2.4 shows the mass of hot gas accumulated inside a bubble for different resolutions of 1D spherically symmetric FLASH simulations with and without cooling and heat conduction. We can see that simulations with lower resolution have less mass accumulated inside the bubble. Although the accumulated mass converges for the resolution with 16384 cells or higher, more complex or 3D simulations cannot be performed at such resolutions. The cause of this problem is an unresolved contact discontinuity represented by a single cell with a temperature between 10^4 and 10^7 K. The cooling function peaks around 10^5 K and changes very rapidly around this temperature. Experiments show that on average the lower resolution leads to an overestimation of the cooling; consequently, less mass flows into the bubble interior.

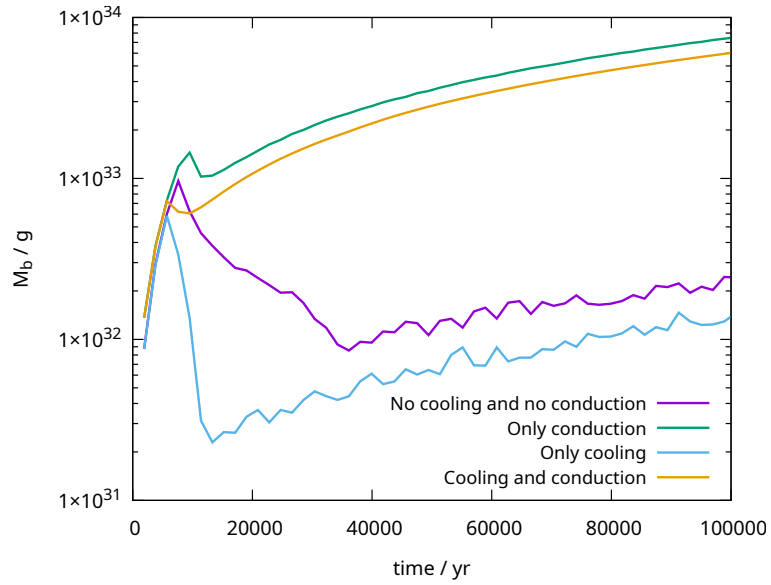


Figure 2.3: Mass M_b of the hot gas in region (b) of the bubble driven by a single star with the mechanical luminosity of the stellar wind $L_w = 1.27 \times 10^{36}$ erg, the terminal velocity $v_\infty = 2 \times 10^8$ cm s $^{-1}$, and the density of the surrounding interstellar medium $n_0 = 1$ cm $^{-3}$ obtained from a 1D spherically symmetric FLASH simulation. Some lines are not perfectly smooth due to errors in the detection of the contact discontinuity. The effect of including or excluding a single cell when calculating the M_b is significant since a cell in spherical coordinates represents a spherical shell. The volume of such a cell scales with r^2 and contributes significantly to the volume of a bubble.

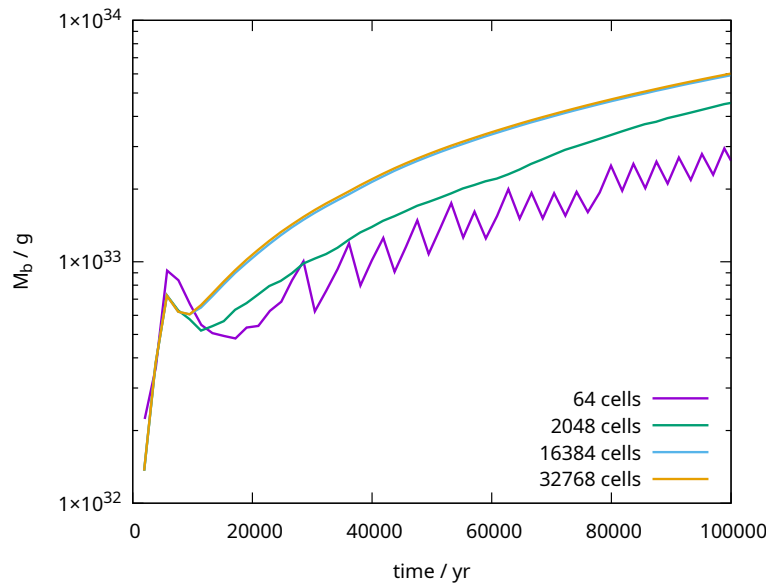


Figure 2.4: Mass M_b of the hot gas in region (b) of the bubble driven by a single star ($L_w = 1.27 \times 10^{36}$ erg) obtained from a 1D spherically symmetric FLASH simulation including cooling and heat conduction.

3. HECTOR – HEat Conduction correctOR

We learned that resolving contact discontinuities in hydrodynamic simulations requires unrealistically high resolutions; consequently, numerical simulations of the interstellar bubbles are not accurate at lower resolutions. To correct this, we developed the HECTOR sub grid model which calculates the correct 1D stationary solution around a contact discontinuity and implemented it in the FLASH hydrodynamic code. We detect problematic areas and use a precalculated table of temperature profiles to correct the solution.

3.1 Semi-analytical model

The model consists of two media—cold and hot¹—separated by a contact discontinuity at $x=0$. The cold medium is defined by its temperature $T(x=0)$, density $\rho(x=0)$, and a hot medium is defined by its temperature $T(x=x_t)$ at a distance x_t from the contact discontinuity. Both media are treated as infinite thermal reservoirs. We seek a time independent solution given by the energy conservation equation.

We need to solve equations 2.1–2.3, which can be expressed in 1D Cartesian coordinates without mass and energy deposition as the system

$$\frac{\partial}{\partial x}(\rho v) = 0, \quad (3.1)$$

$$\rho v \frac{dv}{dx} = -\frac{dp}{dx}, \quad (3.2)$$

$$\frac{\partial}{\partial x} \left(\rho v \left(\frac{1}{2} v^2 + \frac{5}{2} c_s^2 \right) \right) + \frac{\partial q_c}{\partial x} + n_i^2 \Lambda(T) = 0, \quad (3.3)$$

where ρ is the density, p is the pressure, T is the temperature, and v is the velocity of the gas. The pressure is calculated from the ideal gas equation of state

$$p = \frac{k_B \rho T}{\mu m_H}, \quad (3.4)$$

where $\gamma = 5/3$. The speed of sound is defined as

$$c_s^2 = \frac{dp}{d\rho} = \frac{\gamma k_B T}{\mu m_H}. \quad (3.5)$$

The heat flux

$$q_c = -KT^{5/2} \frac{dT}{dx}, \quad (3.6)$$

where $KT^{5/2} \equiv \kappa$ is the heat conduction coefficient given by equation 2.11. Together with the equation of state we can rewrite the conservation laws 3.1–3.3

¹By hot we will refer to gas with temperature equal to or less than 10^4 K.

using a second order differential equation for temperature

$$\rho v \left(v \frac{k_{\text{B}} v}{k_{\text{B}} T - v^2 \mu m_{\text{H}}} + \frac{5\gamma k_{\text{B}}}{2\mu m_{\text{H}}} \right) \frac{dT}{dx} - K T^{5/2} \frac{d^2 T}{dx^2} - \frac{5}{2} K T^{3/2} \left(\frac{dT}{dx} \right)^2 + n^2 \Lambda(T) = 0 \quad (3.7)$$

and an equation for the velocity of the gas

$$\frac{dv}{dx} = \frac{k_{\text{B}} v}{k_{\text{B}} T - v^2 \mu m_{\text{H}}} \frac{dT}{dx}. \quad (3.8)$$

Furthermore, equation 3.1 can be used to express the derivative of the density

$$\frac{d\rho}{dx} = -\frac{\rho}{v} \frac{dv}{dx} = -\frac{\rho}{v} \frac{k_{\text{B}} v}{k_{\text{B}} T - v^2 \mu m_{\text{H}}} \frac{dT}{dx}. \quad (3.9)$$

Finally, equation 3.7 can be expressed using two first order differential equations, which are more suitable for the numerical solution than the second order equation

$$\frac{dT}{dx} = U, \quad (3.10)$$

$$\frac{dU}{dx} = \frac{\rho v}{K T^{5/2}} \left(\frac{k_{\text{B}} v^2}{k_{\text{B}} T - v^2 \mu m_{\text{H}}} + \frac{5\gamma k_{\text{B}}}{2\mu m_{\text{H}}} \right) U - \frac{5}{2T} U^2 + \frac{n_{\text{i}}^2 \Lambda(T)}{K T^{5/2}}. \quad (3.11)$$

We seek a solution of equations 3.8–3.11 with boundary conditions $T(x=0)$, $\rho(x=0)$, and

$$T_{\text{C2}} = \frac{\int_{x_{\text{t}}/2}^{x_{\text{t}}} T(x) \rho(x) dx}{\int_{x_{\text{t}}/2}^{x_{\text{t}}} \rho(x) dx}$$

which is the average temperature in the second half of the solution ($x_{\text{t}}/2 < x < x_{\text{t}}$) corresponding to a single cell in a FLASH simulation. Additionally, the velocity $v(x=0)$ on the cold side of a contact discontinuity can be obtained from equation 3.3. We neglect cooling at $x=0$ because the cooling function is small at low temperatures. The heat flux must be equal to the mechanical energy flux (Cowie and McKee [1977])

$$\rho v \left(\frac{1}{2} v^2 + \frac{5}{2} c_{\text{s}}^2 \right) = -q_{\text{c}} \quad \text{for } x=0. \quad (3.12)$$

There is only one real solution for $v(x=0)$. We can discard the other two solutions with imaginary components as non-physical.

We solve equations 3.8–3.11 numerically. We start on the cold side where $x=0$. We guess an initial value of $\frac{dT}{dx}(x=0)$. Then we integrate numerically using the fourth-order Runge–Kutta method until we reach x_{t} . Then we calculate T_{C2} and compare it to the temperature T_{t} in the cell² on the hot side of the contact discontinuity. If the values are different, we use the bisection method and repeat the process with different values of $\frac{dT}{dx}(x=0)$ until we get $T_{\text{C2}} \approx T_{\text{t}}$.

Figure 3.1 shows a comparison between a semi-analytical solution and a high resolution (256 cells for a single contact discontinuity) FLASH simulation. The boundary conditions are implemented in FLASH by changing the values of the

²Cell in a FLASH simulation using the results from HECTOR to improve its solution on the contact discontinuity.

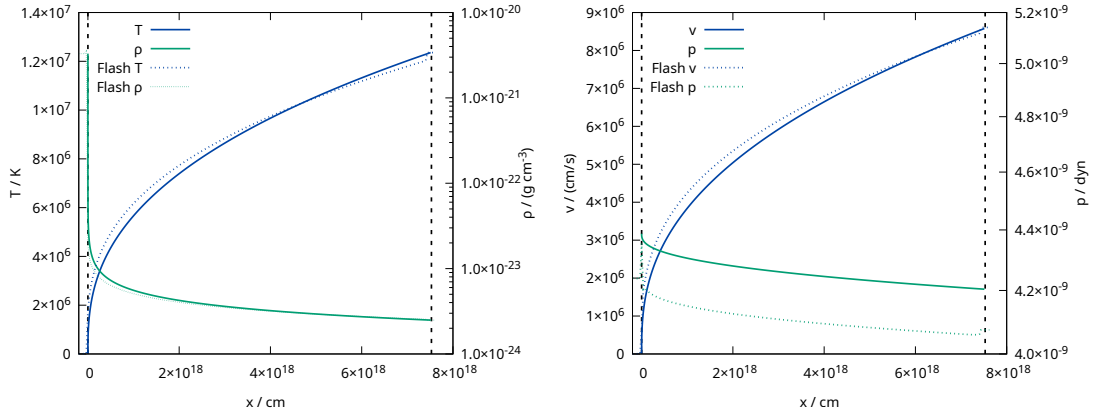


Figure 3.1: Comparison of a semi-analytical solution with a FLASH solution. Boundary conditions are set to $\rho(x = 0) \doteq 3.3 \times 10^{-21} \text{ g cm}^{-3}$, $T(x = 0) = 9.7 \times 10^3 \text{ K}$, and $T_t = 1.24 \times 10^7 \text{ K}$.

first and last few cells in each step. We can see that the agreement between the two solutions is particularly good³. The small differences are due to the fact that the FLASH solution is not completely stationary and shows oscillations in time due to imperfections in the implementation of the boundary conditions.

3.2 Correcting FLASH solution

A contact discontinuity is characterized by a significant rise in temperature and a drop in density. To detect contact discontinuities in FLASH, we calculate the product of the normalized gradients of temperature and density in each cell and direction. Any cell with a negative value below a certain threshold is considered as a candidate for a contact discontinuity. We can set this value low enough to detect only unresolved contact discontinuities, since their gradients are even steeper. Empirically, we have found that a value between -0.0001 and -0.1 works well for this threshold when simulating bubbles driven by stars and star clusters. A higher value would give us false positives while a lower value would not detect all contact discontinuities. We will use -0.1 for the threshold to minimize the risk of false positives. If two adjacent cells with the same gradient direction are candidates for a contact discontinuity, only the cell with the lower value (steeper product of the gradients) is used as the contact discontinuity.

Figure 3.2 shows three cells around a contact discontinuity. Temperatures from a FLASH simulation are shown as points. Cell number 2 is marked as the contact discontinuity. We assume that cell number 3 is far enough away from the discontinuity to not be affected by it. We can then use the temperature and density in cell 1 as $T(x = 0)$ and $\rho(x = 0)$, respectively, and the temperature in cell 3 as T_t , and find a more detailed solution using the semi-analytical model, shown in the figure as a dashed line. Finally, we set the temperature in cell two to the value obtained from the semi-analytical solution. It would not be possible to calculate a semi-analytical solution every time a contact discontinuity is detected

³Note that the pressure is almost constant in both solutions resulting in a fine scale in the figure. Both solutions differ by less than 4%.

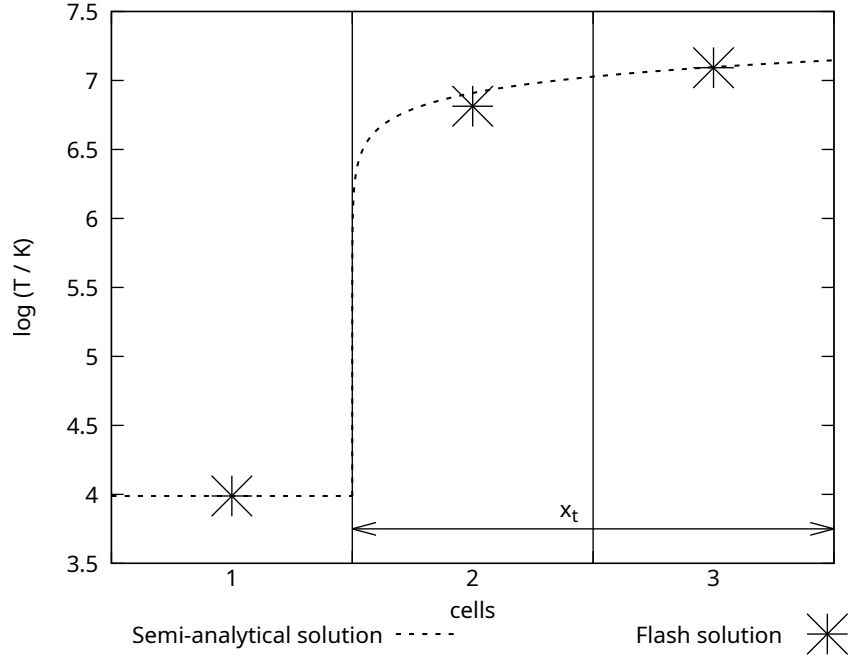


Figure 3.2: Points represent temperatures in 3 cells surrounding a contact discontinuity in a FLASH simulation. Dashed line shows semi-analytical solution with a much higher resolution.

in FLASH. Instead, we interpolate in precalculated values from table 3.1 and set the results as temperatures in cells with detected contact discontinuities. The table has four parameters: the distance from the contact discontinuity x_t given by the cell size, the density of the cold gas at the contact discontinuity $\rho(x = 0)$, the temperature of the cold gas at the contact discontinuity $T(x = 0)$; and the temperature of the hot gas averaged over a cell at distance $0.75x_t$ from the contact discontinuity. It covers the relevant part of the parametric space for interstellar bubbles where solutions exist. In addition, we turn off cooling in cells with modified temperature, since its effects are already included in the semi-analytical solution.

Table 3.1: Precalculated solutions used to correct temperature at contact discontinuities in FLASH simulations.

$\frac{x_t}{\text{cm}}$	$\frac{\rho(x=0)}{\text{g cm}^{-3}}$	$\frac{T(x=0)}{\text{K}}$	$\frac{T_{C2}}{\text{K}}$	$\frac{T_{C1}}{T_{C2}}$	$\frac{dT}{dx}(x=0)$ K cm^{-1}
2.00×10^{17}	1.00×10^{-21}	1000	1000000	0.53	7.65×10^{-8}
2.00×10^{17}	1.00×10^{-21}	2000	1000000	0.55	1.96×10^{-8}
2.00×10^{17}	2.50×10^{-21}	1000	1000000	0.57	3.68×10^{-8}
2.00×10^{17}	7.50×10^{-22}	600	1000000	0.51	1.81×10^{-7}
4.00×10^{17}	1.00×10^{-21}	1000	1000000	0.55	2.80×10^{-8}
4.00×10^{17}	1.00×10^{-21}	8000	2500000	0.54	1.67×10^{-8}
4.00×10^{17}	2.50×10^{-21}	2000	2500000	0.52	1.44×10^{-7}
4.00×10^{17}	2.50×10^{-21}	4000	2500000	0.55	4.47×10^{-8}
4.00×10^{17}	5.00×10^{-21}	8000	5000000	0.53	1.01×10^{-7}
\vdots	\vdots	\vdots	\vdots	\vdots	\vdots
1.28×10^{20}	7.50×10^{-24}	4000	2500000	0.54	1.41×10^{-10}
1.28×10^{20}	7.50×10^{-24}	4000	2500000	0.55	1.38×10^{-10}
1.28×10^{20}	7.50×10^{-24}	6000	2500000	0.56	6.41×10^{-11}
1.28×10^{20}	7.50×10^{-24}	600	1000000	0.58	8.91×10^{-11}
1.28×10^{20}	7.50×10^{-24}	8000	2500000	0.57	3.40×10^{-11}
1.28×10^{20}	7.50×10^{-24}	8000	2500000	0.57	3.34×10^{-11}

4. Results

We have performed several FLASH simulations to determine how temperature correction at the contact discontinuity affects the structure and the evolution of the interstellar bubbles. All 3D simulations use the Cartesian coordinate system while 1D spherically symmetric simulations use spherical geometry. We use the results of the HECTOR code, which uses the Cartesian coordinates, for simulations with spherical geometry because the contact discontinuities are small compared to the scales at which their shape changes, and far enough from the center that the geometry is close to Cartesian.

4.1 Setup

All simulations start with a domain filled with uniform gas characterized by a particle number density n_{ISM} and temperature T_{ISM} . Both radiative cooling and heat conduction are enabled. A source of the stellar wind with mechanical luminosity L_w and terminal velocity v_∞ is placed in the center. The source is implemented as a sphere with a cut-off radius R_{cut} into which the mass and the thermal energy are inserted following the generalized Schuster profile (Ninkovic [1998])

$$\rho_S(r) = N \left(1 + \frac{r}{R_c}\right)^{-\beta} \quad \text{for } r < R_{\text{cut}}, \quad (4.1)$$

where r is the radius measured from the center, R_c is the core radius, the slope $\beta = 1.5$, and N is a normalization constant such that $\int_0^{R_c} 4\pi r^2 \rho_S(r) dr = 1$. The mass deposition rate is

$$q_m(r) = \rho_S(r) \dot{m}_w, \quad (4.2)$$

where \dot{m}_w is the total mass of the wind inserted per a unit of time and the energy deposition rate is

$$q_e(r) = \rho_S(r) L_w. \quad (4.3)$$

For all 3D simulations, we set the boundary conditions to outflow, which means that gas is allowed to move freely out of the computational domain, but no gas enters the domain from outside. In the case of the 1D simulations, we also set the outer boundary condition to outflow, but the inner boundary condition (at $r = 0$) is set to reflect, which ensures that no gas passes this boundary. All of our simulations use a uniform grid.

4.2 Single star

First, we simulated a bubble driven by a star with $L_w = 1.27 \times 10^{36}$ erg, $v_\infty = 2000 \text{ km s}^{-1}$, $R_c = 0.13 \text{ pc}^1$, and $R_{\text{cut}} = 0.39 \text{ pc}$. We used the same values as Weaver et al. [1977] so that we can easily compare the results. The surrounding interstellar medium has $n_{\text{ISM}} = 1 \text{ cm}^{-3}$ and $T_{\text{ISM}} = 10^4 \text{ K}$. For 1D simulations we

¹The core radius is much larger than the size of the star because we need to insert the wind into multiple cells even at lower resolutions.

use a computational domain with a radius of 10 pc while for 3D simulations we use a domain of 20 pc across in all 3 directions.

Here we show how the HECTOR code improves the convergence with the resolution of the mass M_b of the hot ($T > 3 \times 10^5$ K) shocked stellar wind accumulated in region (b). Figure 4.1 shows M_b as a function of time. The low resolution (64 cells) 1D simulation without HECTOR underestimates M_b by a factor of $\sim 2 - 3$ compared to the high resolution (32768 cells) simulation. This is consistent with our results presented in figure 2.4, where we show that M_b depends on the resolution of the simulation. With HECTOR, both low and high resolution 1D and 3D simulations give consistent results that agree with the results of the high resolution simulation without HECTOR.

We ran two 3D simulations with the HECTOR code at resolutions of 128^3 (low) and 512^3 (high). The low resolution 3D simulation differs from the higher resolution simulations in the early stages. This is due to the small forming structure not being properly resolved². Figure 4.3 shows a comparison between the 3D simulations of the two high-resolution runs with (bottom) and without (top) HECTOR. A single time frame showing the gas density in a plane of cells at $z = 0$ is displayed. Figure 4.4 shows a comparison of the high and low resolution 3D simulations with HECTOR. In summary, we can see that the HECTOR code significantly improves the convergence of M_b with the resolution.

Figure 4.2 shows a comparison of the 1D spherically symmetric solution with 2048 cells and HECTOR with the semi-analytical Weaver et al. [1977] solution calculated with Schure et al. [2009] cooling. The computational domain has a radius of 80 pc to cover a significant fraction of the bubble evolution, i.e., it is 8 times larger than for the simulations shown in figure 4.1. As a result, the effective resolution of this simulation, i.e., the grid cell size, is similar to that of the 256 cell simulation in figure 4.1. We can see an excellent agreement in the bubble expansion between the two models: the radius R_2 is practically identical in both solutions. The mass M_b and the thermal energy in region (b), E_b , grow slightly faster in the FLASH simulations. This may be due to a different value of the constant K in the heat conduction coefficient used by Weaver et al. [1977]. In addition, Weaver et al. [1977] introduce several simplifying assumptions to make the derivation possible, which may lead to minor differences in the results. However, we can see that the HECTOR code significantly improves the agreement between the low resolution FLASH simulation and the semi-analytic Weaver solution. The figure also includes a FLASH simulation without HECTOR. We see that not only the mass M_b and luminosity L_b are lower without HECTOR, but also the radius of the outer shock front R_2 is smaller. At 3.8 Myr, the simulation with the unresolved contact discontinuity has a 25% smaller radius of the bubble.

4.3 Star cluster

As a further test, we run simulations of a bubble created by a star cluster embedded in a molecular cloud, to cover also this astrophysically interesting part

²3D simulations require twice the resolution compared to 1D simulations because the source is in the center of the computational domain compared to the 1D spherically symmetric simulation where we place the source at $r = 0$ and calculate the solution only for $r \geq 0$.

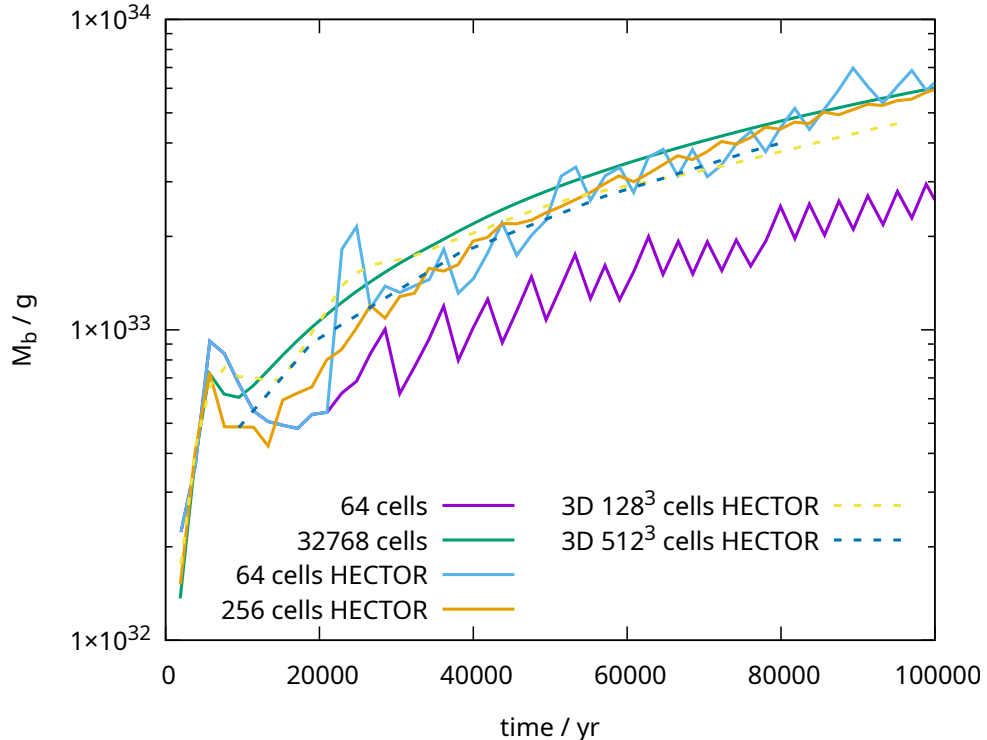


Figure 4.1: Mass M_b of the hot gas in the region (b) of the bubble driven by a single star ($L_w = 1.27 \times 10^{36}$ erg). Different curves show simulations in 1D or 3D, at low or high resolution, and with or without HECTOR, as indicated by the inset labels.

of the parameter space. We treat the cluster as the source of the stellar wind, with $L_w = 3 \times 10^{38}$ erg, $v_\infty = 2000$ km s $^{-1}$, $R_c = 1.0$ pc, and $R_{\text{cut}} = 3.0$ pc. The above L_w corresponds to about 100 massive stars, i.e., the star cluster of mass $\sim 10^4 M_{\text{Sun}}$, assuming the standard stellar initial mass function. The uniform ambient medium has a density of 10^3 cm $^{-3}$ and a temperature of 100 K, which are typical conditions inside molecular clouds. For 1D simulations we use a computational domain with a radius of 50 pc, while for 3D simulations we use a domain of 67 pc across in all 3 directions.

For the star cluster, we present only the convergence tests, since the Weaver solution with these parameters is not available. Figure 4.5 shows M_b as a function of time. First, we see that without HECTOR M_b depends on the resolution. Simulations of the star cluster require shorter time steps and about ten times longer simulation time compared to simulations with a single star; consequently, we were unable to verify that the accumulated mass converges at high enough resolution. With HECTOR, 1D simulations yield consistent results regardless of resolution. Both low and high resolution 3D simulations with HECTOR yield smaller M_b compared to 1D simulations, but significantly larger M_b compared to simulations without HECTOR, making them much closer to the converged high resolution 1D simulation. 3D simulations with HECTOR give consistent results for different resolutions and the correction brings the results closer to 1D simulations with HECTOR.

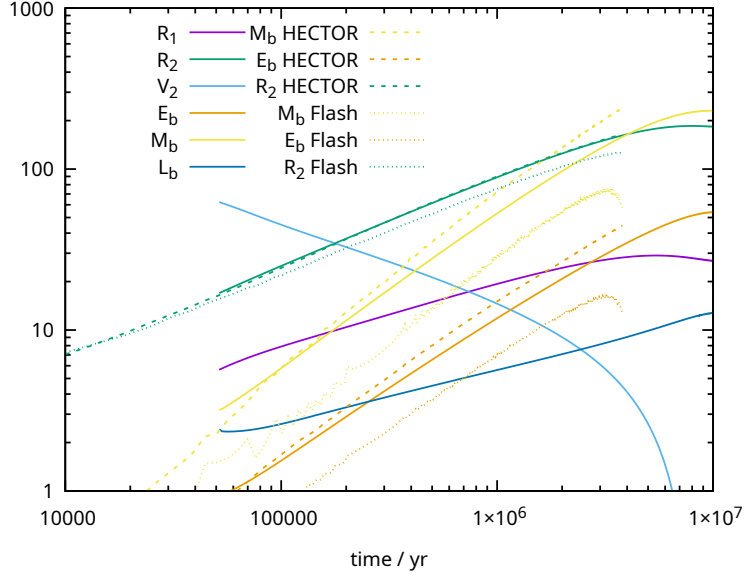


Figure 4.2: Evolution of a bubble driven by a single star ($L_w = 1.27 \times 10^{36}$ erg). Results from Weaver et al. [1977] compared to 1D FLASH simulations with and without HECTOR. The individual lines show the radius of the reverse shock, R_1 (magenta), the radius of the outer shock front, R_2 (green), the shock velocity, V_2 (light blue), the thermal energy in region (b), E_b (orange), the mass of the hot gas in region (b), M_b (yellow), and the luminosity of region (b), L_b (dark blue).

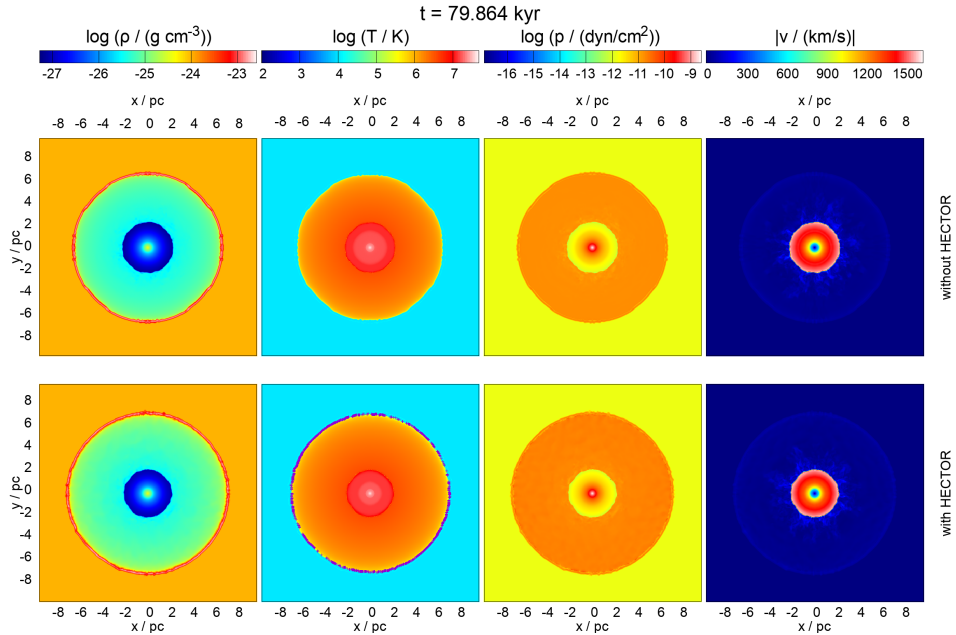


Figure 4.3: Bubble driven by a single star ($L_w = 1.27 \times 10^{36}$ erg). Individual panels show by color the following quantities (from left to right) in the plane $z = 0$ at time 80 kyr: logarithm of the gas density, logarithm of the gas temperature, logarithm of the gas pressure and the magnitude of the gas velocity. The top row shows results without HECTOR, the bottom row shows a simulation with HECTOR. Purple points in the temperature mark where a contact discontinuity was detected, and the temperature was modified.

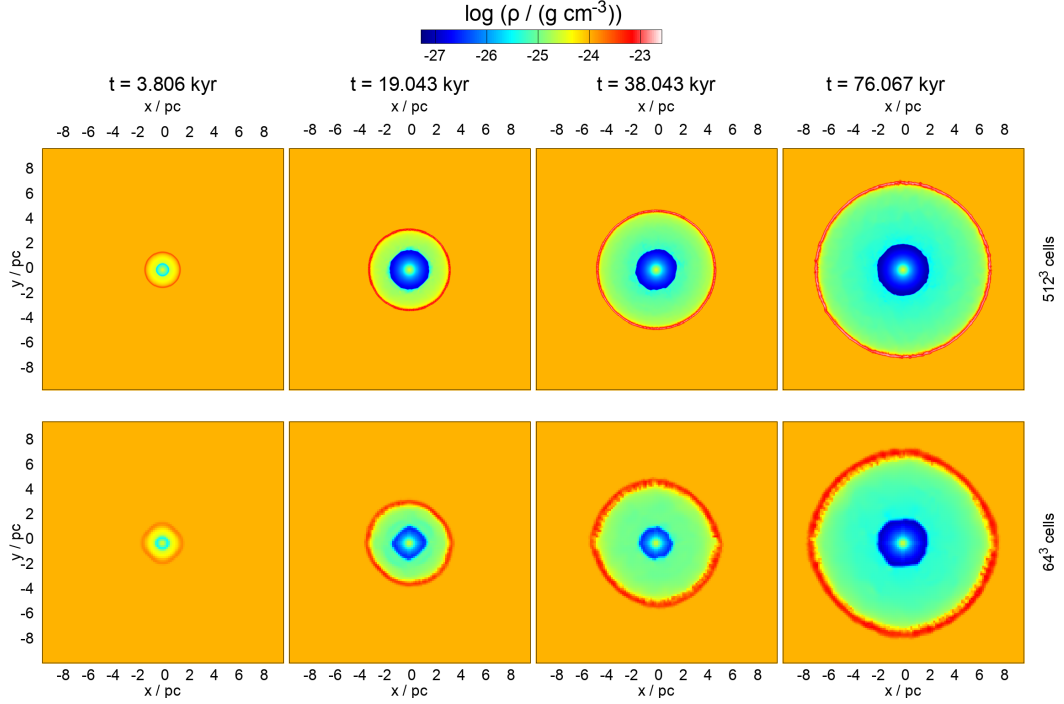


Figure 4.4: Bubble driven by a single star ($L_w = 1.27 \times 10^{36}$ erg). The top row shows results with 512^3 cells and the bottom row with 128^3 cells. Individual panels show the logarithm of the gas density at plane $z = 0$ at times 4, 19, 38 and 76 kyr from the beginning of the expansion.

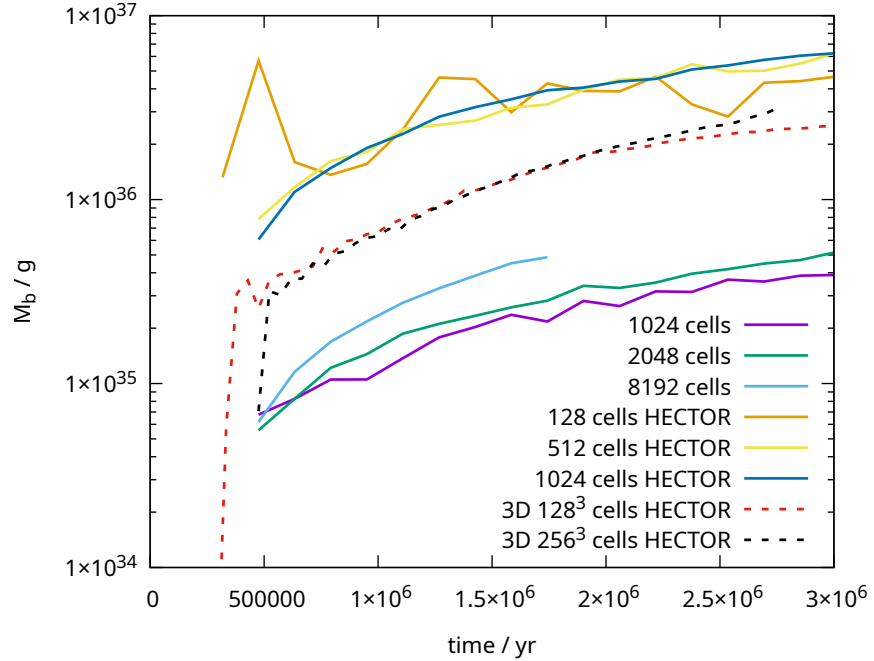


Figure 4.5: Mass M_b of the hot gas in region (b) of the bubble driven by a star cluster ($L_w = 3 \times 10^{38}$ erg). The surrounding interstellar medium has $n_{\text{ISM}} = 1000 \text{ cm}^{-3}$ and $T_{\text{ISM}} = 100 \text{ K}$.

Summary

We have studied interstellar bubbles by means of hydrodynamic simulations including the effects of heat conduction and radiative cooling. When using either radiative cooling or heat conduction everything works as expected but when we enable both processes at the same time the solution is inaccurate at lower resolution due to the unresolved high temperature gradients at the contact discontinuity. This leads to a lower evaporation flux from the shell into the region of the shocked stellar wind. As a result, less mass accumulates in the bubble interior, and this affects the bubble dynamics (e.g., the expansion rate). To resolve the contact discontinuity, we need 1D simulations with resolutions that cannot be reproduced in 3D due to prohibitively high computational costs. With higher mechanical luminosities of the stellar wind, such as in star clusters, we have not been able to perform the 1D simulations at resolutions high enough to resolve the contact discontinuity.

We have developed the HECTOR code to solve the above problem. It consists of a semi-analytic model for finding detailed 1D stationary solutions of contact discontinuities and a module for the hydrodynamic code FLASH to correct simulations on the fly. Within FLASH we detect problematic regions using normalized gradients of density and temperature. When an unresolved contact discontinuity is detected, a precalculated table of temperature profiles from HECTOR is used to correct the solutions.

With HECTOR, simulations of interstellar bubbles around single stars give the same results at different resolutions and in both 1D and 3D. The solutions are also consistent with results by Weaver et al. [1977].

Interstellar bubbles around star clusters give consistent results at different resolutions with HECTOR. In 3D simulations less mass accumulates in the hot region of the shocked stellar wind than in 1D simulations. We believe that HECTOR improves both 1D and 3D simulations, but more work needs to be done to determine the correct solution for the evolution of bubbles driven by star clusters.

In the future, we hope to use HECTOR in complex simulations of the interstellar medium in galaxies, in particular in the SILCC project (Simulating the Life-Cycle of molecular Clouds)—a large international collaboration aiming to improve our understanding of the star-gas cycle in galaxies (Walch et al. [2015]).

Bibliography

- V. S. Avedisova. Formation of Nebulae by Wolf-Rayet Stars. *Soviet Ast.*, 15: 708, April 1972. URL <https://ui.adsabs.harvard.edu/abs/1972SvA...15..708A>.
- J. Castor, R. McCray, and R. Weaver. Interstellar bubbles. *ApJ*, 200:L107–L110, September 1975. doi: 10.1086/181908. URL <https://ui.adsabs.harvard.edu/abs/1975ApJ...200L.107C>.
- NASA Goddard Space Flight Center. Hubble sees a star ‘inflating’ a giant bubble, Apr 2016. URL <https://www.flickr.com/photos/gsfrc/26534662246/>.
- E. Churchwell, M. S. Povich, D. Allen, M. G. Taylor, M. R. Meade, B. L. Babler, R. Indebetouw, C. Watson, B. A. Whitney, M. G. Wolfire, T. M. Bania, R. A. Benjamin, D. P. Clemens, M. Cohen, C. J. Cyganowski, J. M. Jackson, H. A. Kobulnicky, J. S. Mathis, E. P. Mercer, S. R. Stolovy, B. Uzpen, D. F. Watson, and M. J. Wolff. The Bubbling Galactic Disk. *ApJ*, 649(2):759–778, October 2006. doi: 10.1086/507015. URL <https://ui.adsabs.harvard.edu/abs/2006ApJ...649..759C>.
- P. Colella and Paul R. Woodward. The Piecewise Parabolic Method (PPM) for Gas-Dynamical Simulations. *Journal of Computational Physics*, 54:174–201, September 1984. doi: 10.1016/0021-9991(84)90143-8. URL <https://ui.adsabs.harvard.edu/abs/1984JCoPh...54..174C>.
- L. L. Cowie and C. F. McKee. The evaporation of spherical clouds in a hot gas. I. Classical and saturated mass loss rates. *ApJ*, 211:135–146, January 1977. doi: 10.1086/154911. URL <https://ui.adsabs.harvard.edu/abs/1977ApJ...211..135C>.
- L. Deharveng, F. Schuller, L. D. Anderson, A. Zavagno, F. Wyrowski, K. M. Menten, L. Bronfman, L. Testi, C. M. Walmsley, and M. Wienen. A gallery of bubbles. The nature of the bubbles observed by Spitzer and what ATLASGAL tells us about the surrounding neutral material. *A&A*, 523:A6, November 2010. doi: 10.1051/0004-6361/201014422. URL <https://ui.adsabs.harvard.edu/abs/2010A&A...523A...6D>.
- Kareem El-Badry, Eve C. Ostriker, Chang-Goo Kim, Eliot Quataert, and Daniel R. Weisz. Evolution of supernovae-driven superbubbles with conduction and cooling. *MNRAS*, 490(2):1961–1990, December 2019. doi: 10.1093/mnras/stz2773. URL <https://ui.adsabs.harvard.edu/abs/2019MNRAS...490.1961E>.
- B. Fryxell, K. Olson, P. Ricker, F. X. Timmes, M. Zingale, D. Q. Lamb, P. MacNeice, R. Rosner, J. W. Truran, and H. Tufo. Flash: An adaptive mesh hydrodynamics code for modeling astrophysical thermonuclear flashes. *ApJS*, 131(1):273–334, November 2000. doi: 10.1086/317361. URL <https://ui.adsabs.harvard.edu/abs/2000ApJS...131..273F>.

- Sam Geen, Joakim Rosdahl, Jeremy Blaizot, Julien Devriendt, and Adrienne Slyz. A detailed study of feedback from a massive star. *MNRAS*, 448(4):3248–3264, April 2015. doi: 10.1093/mnras/stv251. URL <https://ui.adsabs.harvard.edu/abs/2015MNRAS.448.3248G>.
- Message Passing Interface Forum. *MPI: A Message-Passing Interface Standard Version 4.0*, June 2021. URL <https://www.mpi-forum.org/docs/mpi-4.0/mpi40-report.pdf>.
- S. Ninkovic. On the Generalised Schuster Density Law. *Serbian Astronomical Journal*, 158:15, January 1998. URL <https://ui.adsabs.harvard.edu/abs/1998SerAJ.158...15N>.
- K. M. Olson, P. MacNeice, B. Fryxell, P. Ricker, F. X. Timmes, and M. Zingale. PARAMESH: A Parallel, Adaptive Mesh Refinement Toolkit and Performance of the ASCI/FLASH code. In *American Astronomical Society Meeting Abstracts*, volume 195 of *American Astronomical Society Meeting Abstracts*, page 42.03, December 1999. URL <https://ui.adsabs.harvard.edu/abs/1999AAS...195.4203O>.
- Tim-Eric Rathjen, Thorsten Naab, Philipp Girichidis, Stefanie Walch, Richard Wünsch, František Dinnbier, Daniel Seifried, Ralf S. Klessen, and Simon C. O. Glover. SILCC VI - Multiphase ISM structure, stellar clustering, and outflows with supernovae, stellar winds, ionizing radiation, and cosmic rays. *MNRAS*, 504(1):1039–1061, June 2021. doi: 10.1093/mnras/stab900. URL <https://ui.adsabs.harvard.edu/abs/2021MNRAS.504.1039R>.
- K. M. Schure, D. Kosenko, J. S. Kaastra, R. Keppens, and J. Vink. A new radiative cooling curve based on an up-to-date plasma emission code. *A&A*, 508(2):751–757, December 2009. doi: 10.1051/0004-6361/200912495. URL <https://ui.adsabs.harvard.edu/abs/2009A&A...508..751S>.
- L. Spitzer. *Physics of Fully Ionized Gases*. 1962. URL <https://ui.adsabs.harvard.edu/abs/1962pfig.book.....S>.
- J. A. Toalá and S. J. Arthur. Radiation-hydrodynamic Models of the Evolving Circumstellar Medium around Massive Stars. *ApJ*, 737(2):100, August 2011. doi: 10.1088/0004-637X/737/2/100. URL <https://ui.adsabs.harvard.edu/abs/2011ApJ...737..100T>.
- S. Walch, P. Girichidis, T. Naab, A. Gatto, S. C. O. Glover, R. Wünsch, R. S. Klessen, P. C. Clark, T. Peters, D. Derigs, and C. Baczynski. The SILCC (SIMulating the LifeCycle of molecular Clouds) project - I. Chemical evolution of the supernova-driven ISM. *MNRAS*, 454(1):238–268, November 2015. doi: 10.1093/mnras/stv1975. URL <https://ui.adsabs.harvard.edu/abs/2015MNRAS.454..238W>.
- R. Weaver, R. McCray, J. Castor, P. Shapiro, and R. Moore. Interstellar bubbles. II. Structure and evolution. *ApJ*, 218:377–395, December 1977. doi: 10.1086/155692. URL <https://ui.adsabs.harvard.edu/abs/1977ApJ...218..377W>.